



Cite this: *Soft Matter*, 2025,  
21, 2282

## Hybrid phytoglycogen-dopamine nanoparticles as biodegradable underwater adhesives†

JIAYI LIU,<sup>a</sup> DMITRII SYCHEV,<sup>a</sup> NADIIA DAVYDIUK,<sup>a</sup> MAHMoud AL-HUSSEIN,<sup>ab</sup> ANDREAS FERY<sup>ID, a</sup> and QUINN A. BESFORD<sup>ID, \*a</sup>

Developing adhesive materials that can selectively degrade into non-toxic by-products is a key challenge in materials science, particularly for short-term implantable devices and tissue regeneration treatments. Herein, we leverage biodegradable phytoglycogen (PG) nanoparticles (highly branched glucose polysaccharide nanoparticles) as scaffolds for coupling adhesive dopamine motifs to be used as biodegradable underwater adhesives. Phytoglycogen-dopamine (PG-dopa) hybrid nanoparticles could be synthesised in an aqueous solvent, to which the products retained a similar size and particle morphology to the initial PG nanoparticles. The PG-dopa nanoparticles could readily be assembled into dense monolayers on silica substrates through a simple dip-coating procedure. Colloidal probe atomic force microscopy was used to characterise underwater adhesiveness, where it was found that the films produced strain energy release rates approaching  $8 \text{ mJ m}^{-2}$  between hard silica materials. Importantly, the PG-dopa films retained the original biodegradability towards glucosidase enzymes, which can degrade the adhesives in fluids containing these enzymes over time (e.g.,  $45 \text{ U mL}^{-1}$  of  $\alpha$ -amylase solution degraded the majority of the adhesive films in 30 min). Given the inherent biocompatibility of glycogen materials, we anticipate these adhesives having application in short-term implantable devices.

Received 6th December 2024,  
Accepted 16th February 2025

DOI: 10.1039/d4sm01454e

rsc.li/soft-matter-journal

## Introduction

Mussel feet secrete adhesive proteins that help them firmly stick to rocks in marine environments, where the adhesive proteins form plaques on substrates. A linear protein (mfp-5) with an average molecular weight of about 10 kDa plays a significant role in forming robust mussel plaques, especially in the strong interface connection.<sup>1,2</sup> The adhesion ability of mfp-5 is mainly due to L-dopa, which contains a functional catechol group. Hydrogen bonds, metal-coordination and hydrophobic interactions can form between these catechol groups and substrates resulting in strong interface adhesions.<sup>3,4</sup>

These unique underwater adhesive properties of L-dopa have inspired the development of synthetic underwater or wet adhesives, which might find application in the biomedical field. For example, synthetic polymers that mimic mussel adhesive proteins have shown high underwater adhesion strengths.<sup>5–7</sup> Cui *et al.* developed a starch-based tissue adhesive by using dopamine-conjugated starch. This dopamine modified starch

can form a hydrogel when hydrogen peroxide with horseradish peroxidase is used as a cross-linker. Catechol groups served as interfacial adhesion and crosslinking segments.<sup>8</sup> Du *et al.* reported a mechanical and chemical robust coating using catechol-modified polyallylamine. The catechol group and amine group contribute to the strong interface adhesion on several substrates and cohesive interaction by forming covalent bonds. The abundant amine groups on the coating provide grafting sites for secondary modification.<sup>9</sup> Whilst these materials have demonstrated unique adhesive properties, there is interest in moving towards minimally synthetic, bio-sourced materials as adhesives. Furthermore, for applications involving bio-contact (e.g., implants and tissue adhesives), biocompatibility is necessary. Glycogen is an interesting material in this regard, which has been gaining momentum in various applications,<sup>10</sup> particularly as it has been shown to induce minimal inflammation, coagulation, and interactions with the immune system in human blood.<sup>11</sup>

Glycogen is a randomly hyperbranched polysaccharide nanoparticle that can be obtained from various sources (animals, tissues, and plants). Its structure consists of repeating D-glucose units connected by linear  $\alpha$ -(1,4) glycosidic linkages, with branching via  $\alpha$ -(1,6) glycosidic linkages. The nanoparticle size, molecular weight, degree of branching and content of proteins are different depending on the source. For instance, phytoglycogen (PG) derived

<sup>a</sup> Leibniz-Institut für Polymerforschung Dresden e. V., Hohe Str. 6, 01069 Dresden, Germany. E-mail: besford@ipfdd.de

<sup>b</sup> Physics Department, The University of Jordan, Amman 19942, Jordan

† Electronic supplementary information (ESI) available. See DOI: <https://doi.org/10.1039/d4sm01454e>



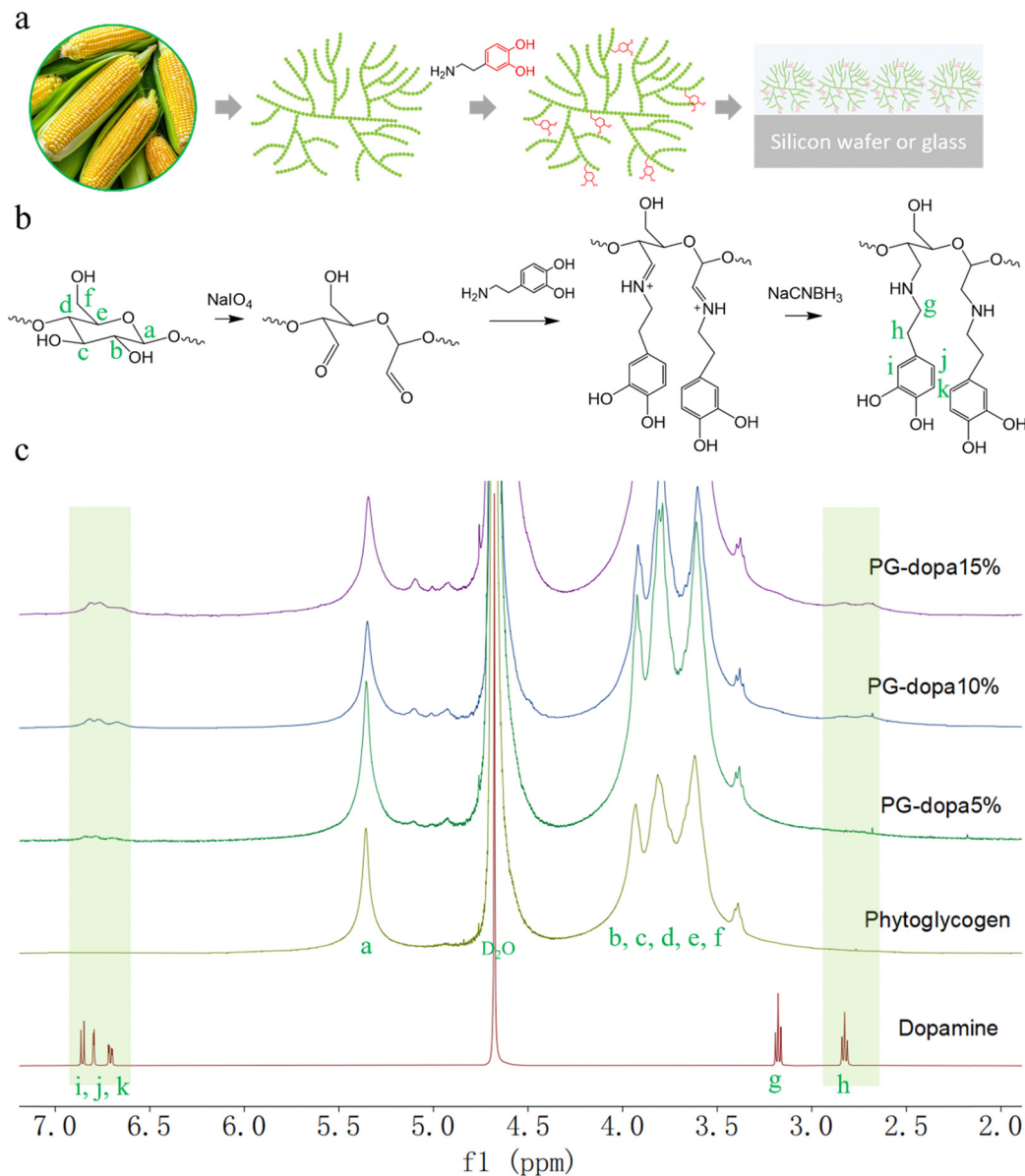


**Fig. 1** (a) Phytoglycogen (PG) extracted from sweet corn and monolayer dopamine-conjugated phytoglycogen (PG-dopa) on substrates. (b) The synthesis scheme of PG-dopa. (c) <sup>1</sup>H NMR (600 MHz, D<sub>2</sub>O) spectra of dopamine, PG, PG-dopa5%, PG-dopa10% and PG-dopa15%.

from sweet corn has a diameter of  $\sim 80$  nm in water and a high molecular weight of 20 MDa<sup>12</sup> (Fig. 1(a)). The hydroxyl groups on glycogen can be modified to produce other functional groups, such as carboxylic acid groups,<sup>13</sup> quaternary ammonium groups,<sup>14</sup> and allyl groups,<sup>15</sup> as examples. The glucose residues can be oxidized to produce an aldehyde group, which can further react with primary amines to conjugate functional groups.<sup>16</sup> Previous works have investigated thiolated glycogens as mucosal adhesives and as gold-adhering nanoparticles,<sup>17</sup> which have demonstrated the robust properties of adhesive glycogen. Coupling the unique properties of glycogen with underwater adhesive catechol motifs has not been pursued, to our best knowledge.

Herein, we report a rapid, straightforward method to form underwater PG adhesive coatings using PG-dopamine (PG-dopa)

hybrids, inspired by the mussel foot protein (Fig. 1(a)). PG nanoparticles, which are sourced from plants (sweet corn kernels), are hydrophilic and have no ability to adhere to underwater substrates.<sup>17</sup> However, we found that PG-dopa nanoparticles show remarkable affinity to silicon dioxide surfaces. A homogenous coating consisting of single layer PG-dopa nanoparticles can be formed by simply dip coating into PG-dopa dispersions. The PG-dopa coating showed great adhesiveness to underwater silicon dioxide materials. The maximum average adhesion energy reached  $7.20 \text{ mJ m}^{-2}$ . Previously, values as high as  $2.64 \text{ mJ m}^{-2}$  were reported for dopa-containing mussel-inspired proteins.<sup>18</sup> The modification of dopamine did not affect the biodegradability of PG-dopa nanoparticles or coatings. We anticipate these adhesives to have use in short-term implantable devices.

## Methods

### Materials

Phytoglycogen (PG) sourced from the kernels of sweet corn was purchased from Mirexus (Guelph, Canada). Sodium periodate ( $\geq 99.8\%$ ), dopamine hydrochloride ( $\geq 98\%$ ), sodium cyanoborohydride ( $\geq 95\%$ ), 4-methylcatechol ( $\geq 95\%$ ),  $\alpha$ -amylase (powder,  $\sim 30$  U  $\text{mg}^{-1}$ ), phenol ( $\geq 99\%$ ) and deuterium oxide ( $\geq 99.9\%$ ) were purchased from Sigma-Aldrich. Sulfuric acid ( $\geq 95\%$ ) was purchased from Fisher Chemical. Absolute ethanol was purchased from VWR chemicals. Methyl sulfoxide ( $99.7 + \%$ ) was purchased from Thermo Scientific. The dialysis tube (14 000 Daltons cut-off) was purchased from BioDesign Inc. of New York. High-purity (Milli-Q) water with a resistivity of  $18.2\text{ M}\Omega\text{ cm}$  was obtained from a Direct-Q<sup>®</sup> 3UV water purification system (Merck Chemicals GmbH, German).

### Synthesis of PG-dopa

PG-dopa was synthesized by the Schiff base reaction between dopamine and oxidized PG and then reduced by sodium cyanoborohydride. We synthesized some different conjugates (percentage modifications of PG). Here, we describe the 10% modification (10% of glucose units of PG modified). PG (0.2433 g, 1.50 mmol) was dispersed in 10 mL of Milli-Q water by ultrasonication. Then, sodium periodate (0.0321 g, 0.15 mmol) was added and the dispersion was stirred for 2 h at room temperature in the dark. The dispersion was dialyzed (14 kDa cutoff) against Milli-Q water one night to remove the oxidizing agent. The dispersion was transferred to a round bottom flask. The flask was sealed by a rubber septum and degassed with argon for 20 minutes. Dopamine hydrochloride (0.0569 g, 0.30 mmol) was dissolved in 5 mL of phosphate buffer (0.1 M, pH 5) and was added to the oxidized PG dispersion. After 4 h, sodium cyanoborohydride (0.0471 g, 0.75 mmol) was dissolved in 5 mL of phosphate buffer (0.1 M, pH 5) and was added to the reaction dispersion for one night. Subsequently, the dispersion was precipitated in 40 mL of ethanol twice. The precipitate dispersed in 20 mL of Milli-Q water again and dialyzed (14 kDa cut-off) against Milli-Q water for 3 days. Finally, the dispersion was freeze-dried to obtain the PG-dopa10%. The degree of conjugation was determined by the  $^1\text{H}$  NMR spectrum and catechol group assay.

### Nuclear magnetic resonance spectroscopy (NMR)

$^1\text{H}$  spectra were collected using an Avance III HD 500 MHz spectrometer (Bruker, Germany). Deuterium oxide ( $\text{D}_2\text{O}$ ) was used as the solvent.

### Catechol group assay

The UV-vis absorbance spectra were recorded on a SPECORD 40 spectrophotometer (Analytik Jena, Germany) and analyzed using the software WinASPECT. Spectra were acquired with a scan speed of  $20\text{ nm s}^{-1}$ . A constant of  $0.005\text{ mg mL}^{-1}$  iron(III) chloride solution, the 4-methylcatechol solution concentration range from  $0.01\text{ mg mL}^{-1}$  to  $0.08\text{ mg mL}^{-1}$  and the total volume of 2 mL of carbonate buffer solution (0.1 M, pH 8.3) samples were prepared for the standard absorbance curve. In

detail, a fresh  $0.05\text{ mg mL}^{-1}$  iron(III) chloride and  $1\text{ mg mL}^{-1}$  4-methylcatechol water solution were prepared as stock solutions. To prepare the sample with a 4-methylcatechol concentration of  $0.01\text{ mg mL}^{-1}$ , 0.2 mL of  $0.05\text{ mg mL}^{-1}$  iron(III) chloride solution, 0.02 mL of  $1\text{ mg mL}^{-1}$  4-methylcatechol solution and 1.78 mL of Milli-Q water were added to the PMMA cuvette. The sample with a higher 4-methylcatechol concentration was prepared by increasing the volume of  $1\text{ mg mL}^{-1}$  4-methylcatechol solution and decreasing the volume of Milli-Q water. The volume of  $0.05\text{ mg mL}^{-1}$  iron(III) chloride solution and the total volume were always 0.2 mL and 2 mL. The cuvettes were placed in the chamber for the measurement after the solution became homogeneous. A wavelength range from 300 to 800 nm was used.

The PG-dopa5%, PG-dopa10% and PG-dopa15% nanoparticles were dispersed in carbonate buffer solution (0.1 M, pH 8.3) with the help of ultrasonication for 30 minutes. All the concentrations were  $0.8\text{ mg mL}^{-1}$ . To prepare the PG-dopa samples for the UV-vis spectrometer, 0.2 mL of  $0.05\text{ mg mL}^{-1}$  iron(III) chloride solution and 1.8 mL of  $0.8\text{ mg mL}^{-1}$  PG-dopa5% or PG-dopa10% or PG-dopa15% solution was added to the cuvette. The cuvettes were placed in the chamber for the measurement after the solution became homogeneous. A wavelength range from 300 to 800 nm was used.

To compare the absorbance intensity of PG-dopa samples with the 4-methylcatechol standard absorbance curve, the absorbance intensity at a wavelength of 525 nm was used.

### Preparation of the PG-dopa10% coating on a silicon wafer

The PG-dopa10% coating on a silicon wafer was obtained by dip coating in a  $1\text{ mg mL}^{-1}$  PG-dopa10% Milli-Q water dispersion without waiting time. The lift speed was  $0.48\text{ mm s}^{-1}$ . The coated wafer was rinsed with Milli-Q water to remove the unbounded PG-dopa10% nanoparticles.

### Atomic force microscopy (AFM)

AFM topography measurements on nanoparticles and coatings were performed in peak-force mode on a Dimension Fastscan AFM (Bruker, Billerica, MA, USA) with a peak-force set point of 30 mV. A Tap300 Al-G cantilever ( $40\text{ N m}^{-1}$ , 300 kHz, coated by 30 nm Aluminium, BudgetSensors) was employed. All measurements were performed consecutively with the same type of cantilever. The obtained data were processed using Gwyddion software. To obtain the PG and PG-dopa10% nanoparticle AFM topography images,  $0.005\text{ mg mL}^{-1}$  nanoparticle water dispersion was prepared. 0.1 mL of water dispersion was applied to the silicon wafer and dried by slow nitrogen flow. For the thickness of the PG-dopa coating on the silicon wafer, several scratches were prepared using a small syringe needle.

### Dynamic light scattering (DLS)

Hydrodynamic diameters and zeta potential were measured using a Zetasizer Nano-ZS instrument (Malvern Instrument, Malvern, UK). The concentration of both PG and PG-dopa water dispersion was  $1\text{ mg mL}^{-1}$ .



### Scanning electron microscopy (SEM)

SEM images were recorded using a NEON40 SEM (Carl Zeiss Microscopy Deutschland GmbH, Oberkochen, Germany) operated at an acceleration voltage of 1 kV. No additional conductive coating was necessary to prevent charging of the specimen in the electron beam.

### Cryo-transmission electron microscopy (cryo-TEM)

Cryo-TEM images were recorded using a Libra 120 microscope (Carl Zeiss Microscopy Deutschland GmbH, Oberkochen, Germany). 4  $\mu$ L of the specimen was placed onto a holey carbon TEM grid (Quantifoil R3.5/1, 300 mesh), blotted with filter paper and vitrified in liquid ethane at  $-178$  °C using a Grid Plunger (Leica Microsystems GmbH, Wetzlar, Germany). Frozen grids were transferred into a Gatan 626 (Gatan GmbH, München, Germany) cryo-TEM holder. Images were recorded at an accelerating voltage of 120 kV while keeping the specimen at  $-170$  °C.

### X-ray reflectivity

X-ray reflectivity measurements were performed using a XRD 3300 T-T (Seifert) diffractometer with a copper target ( $\lambda = 0.154$  nm). The samples were mounted horizontally at the center of a two-circle goniometer and investigated under specular reflection conditions from 0 to  $6$ °. At specular reflectivity, the scattering vector,  $q = (4\pi/\lambda)\sin\theta$ , was perpendicular to the film ( $z$ -direction), where  $2\theta$  is the scattering angle. Hence, the reflected intensity was sensitive to the electron density profile averaged over the footprint of the incident X-ray beam.

### PG-dopa coating underwater adhesion measurements by colloidal probe AFM

Adhesion measurements were carried out using an atomic force microscope (MFP-3D, Asylum Research, Oxford Instruments, California, USA). The colloidal probe atomic force microscopy (AFM) technique was utilized to measure the adhesion force and quantify adhesion interactions.<sup>19,20</sup> This technique allows quantitative measurements of the adhesion interaction between the adhesive PG-dopa coating and a 20  $\mu$ m diameter silica spherical particle, the colloidal probe. The advantage of using the micrometer size sphere as an indenter is the defined geometry of the contact, unattainable in the case of the hard tip.<sup>21</sup> The borosilicate glass slides with no. 1 thickness (VWR, Radnor, USA) were coated with the adhesive PG-dopa film and used as a sample for the AFM measurements. To fabricate the colloidal probe equipped with a cantilever, the tipless cantilever (CSC 36, Mikromasch Europe, Wetzlar, Germany) was calibrated using the thermal noise technique<sup>22</sup> prior to the attachment of the colloidal probe using a micromanipulator, resulting in a spring constant of 2.51 N m<sup>-1</sup>. Adhesion characterization was carried out by recording the force-distance curves with different maximal loads on the cantilever (50 nN, 100 nN, 215 nN), contact times (0.5–50 s), and retraction rates (100–5000 nm s<sup>-1</sup>). It is worth noting that the retraction rate

was 2000 nm s<sup>-1</sup> unless stated otherwise. The measurement was carried out by recording a 4  $\times$  4 point force map on an arbitrarily chosen position on the sample. For every parameter set, two such force maps were recorded (one for the PG-dopa15% coating). Due to the comparable adhesion of the PG-dopa film between the borosilicate glass substrate and the silica colloidal probe, as the functional groups are the same, the material transfer interfered with the measurements, resulting in the measurement of the cohesion and adhesion interaction mixture. To overcome this issue, the parameters of the measurement were varied in different directions for each of the force maps (*i.e.* for the first set of force maps the load was consecutively increased and for the second set it was consecutively decreased). Within this set, the measured adhesion force (the minimum on the retraction part of the force curve) decreased after several force curves had been recorded. To measure only the adhesive interactions, the values after such drop were omitted, and the cantilever was treated with O<sub>2</sub> plasma to achieve a greater contribution of the adhesion interactions to the measured force.

Adhesion was quantified by integrating the part of the force curve below zero on the retraction part of the force curve and normalising it to the calculated area of contact from maximal deformation within the framework of Johnson–Kendall–Roberts theory.<sup>23</sup> The measurements were conducted at room temperature in Milli-Q water.

### Degradation of PG and PG-dopa nanoparticles by $\alpha$ -amylase solution

The enzymatic degradation of PG and PG-dopa10% was assessed using a phenol–sulfuric acid assay.<sup>11,24</sup> Dispersions of both nanoparticles in Milli-Q water with a concentration of 1 mg mL<sup>-1</sup> were prepared.  $\alpha$ -Amylase was dissolved in PBS buffer (0.01 M, pH 7.4) and the concentration was 1 U mL<sup>-1</sup>. To begin the assay, 70  $\mu$ L of PG or PG-dopa dispersion was added to 200  $\mu$ L of enzyme solution. The resulting solution was incubated at 23 °C with gentle agitation for 3 h. Then, the undigested PG and enzyme were separated from the free glucose using spin columns with a pore size of 10 kDa. The filtrate was collected and divided into sample aliquots of 50  $\mu$ L, to which concentrated sulfuric acid (150  $\mu$ L) was added, followed by addition of 5 wt% phenol water solution. The samples were subsequently incubated at 90 °C with agitation for 20 minutes. The UV-vis absorbance of the digested solution was then measured at 490 nm with an infinite M200 microplate reader (Tecan, Switzerland) using a 96-well plate (Greiner CELLSTAR, Sigma-Aldrich).

To determine the amount of glucose on each particle type, the original PG on each particle type and the original PG solutions (70  $\mu$ L) were each treated with 0.2 M TFA (200  $\mu$ L) for 3 h at 80 °C with agitation. The mixtures were then treated and analyzed as described above for the enzymatic experiments. The extent of degradability was determined as the ratio of UV-vis absorbance reading intensity at 490 nm for the enzymatically degraded particles to the trifluoroacetic acid degraded particles.

## Fluorescence

Fluorescence of the PG-dopa coatings was analysed with a JASCO FP-8500 spectrofluorometer instrument. A quartz surface was cut into a 10 mm strip, and coated with PG-dopa10% nanoparticles. This was then placed inside a quartz cuvette with 4 mL of solution, on a 45° angle to the excitation source, and the detection channel (situated perpendicular to each other). The emission wavelength of the excitation spectrum was 340 nm. The excitation wavelength of the emission spectrum was 280 nm. The excitation wavelength and the emission wavelength for the fluorescence intensity of PG-dopa10% coated quartz over time in the solution of  $\alpha$ -amylase are 280 nm and 310 nm.

## Results and discussion

### Synthesis of PG-dopa

The PG was first oxidized by sodium periodate to produce an aldehyde group.<sup>25</sup> Then, the dispersion was purified by dialysis to remove the oxidizing agent. The aldehyde group in oxidized PG was reacted with the amine of dopamine hydrochloride in phosphate buffer (pH 5.0). Finally, the imine was reduced to a stable secondary amine by reductive amination (Fig. 1(b)).

The successful synthesis and degree of conjugation was confirmed by  $^1\text{H}$  NMR spectroscopy. The i, j and k peaks at  $\delta$  ~ 6.8 ppm were assigned to the protons from the aromatic ring of dopamine, which indicated the presence of the catechol group on the modified nanoparticles (Fig. 1(c)). The methylene protons (g and h) from dopamine hydrochloride can also be found at  $\delta$  3.1 and 2.8 ppm after modification. The degree of conjugation (DC) of dopamine of the PG-dopa was calculated by the equation  $\text{DC} = A_{6.8}/(3 \times A_{5.3})$ , where  $A_{6.8}$  and  $A_{5.3}$  are the integrations of the peak area at  $\delta$  = 6.8 (aromatic protons) and  $\delta$  = 5.3 (the proton at the C1 of glucose repeat unit, a peak), respectively. The DC of different PG-dopa is summarized in Table 1. The number in the term PG-dopa10% is the ratio (mol : mol) of sodium periodate and glucose repeat unit. The degree of conjugation of PG-dopa10% was found to be 4.67%. However, the broadness of the NMR peaks makes absolute quantification difficult for such low conjugation degrees.

Given the broadness of the peaks, the degree of conjugation was additionally confirmed using a catechol assay. 4-Methylcatechol was used to obtain the standard curve over the concentration range of 0.01–0.08 mg mL<sup>-1</sup> (Fig. S1b, ESI<sup>†</sup>). The UV-vis absorbance intensity at a wavelength of 525 nm was used to plot the fitting curve (Fig. S1d, ESI<sup>†</sup>). For the purpose of

**Table 1** Conjugation degrees of PG-dopa determined by  $^1\text{H}$  NMR and the catechol assay

Samples	Degree of conjugation (%)	
	$^1\text{H}$ NMR	Catechol assay
PG-dopa5%	2.67	3.35
PG-dopa10%	4.67	5.22
PG-dopa15%	6.00	7.31

the assay, we assume that the molecular weight of the glucose repeat unit does not change after the conjugation of dopamine. Then, the DC can be calculated by the following equation:

$$\text{DC} = \frac{C_{\text{cat}} \times M_{\text{gru}}}{C_{\text{deg}} \times M_{4\text{mc}}} = 1.6327 \times C_{\text{cat}}$$

where  $C_{\text{cat}}$  is the concentration of the catechol group in the PG-dopa dispersion. Taking the PG-dopa10% for instance,  $C_{\text{cat}}$  is 0.0320 mg mL<sup>-1</sup> from the fitting curve (Fig. S1d, ESI<sup>†</sup>).  $M_{\text{gru}}$  is the molecular weight of the glucose repeat unit in PG, which is 162.1407 g mol<sup>-1</sup>.  $C_{\text{deg}}$  is the concentration of dopamine in the conjugate PG, found to be 0.8 mg mL<sup>-1</sup> in this experiment.  $M_{4\text{mc}}$  is the molecular weight of 4-methylcatechol and is 124.1372 g mol<sup>-1</sup>. The DC of PG-dopa5%, PG-dopa10% and PG-dopa10% were 3.35%, 5.22% and 7.31% (Table 1).

### Characterization of PG and PG-dopa nanoparticles

Atomic force microscopy (AFM) was used to measure the dry state morphology and height of PG and PG-dopa10% nanoparticles (Fig. 2(a) and (b), respectively). The height of both PG and PG-dopa10% nanoparticles was ~12 nm from AFM

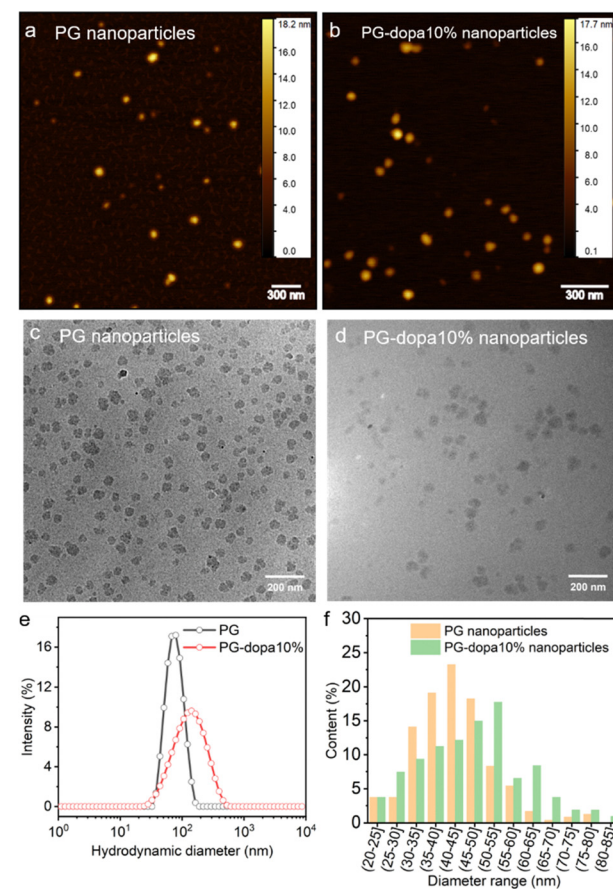


**Fig. 2** (a) Dry state AFM topography image of PG nanoparticles. (b) Dry state AFM topography image of PG-dopa nanoparticles. (c) TEM image of PG nanoparticles. (d) TEM image of PG-dopa10% nanoparticles. (e) DLS hydrodynamic diameter populations of PG and PG-dopa nanoparticles. (f) Calculated diameter range populations of PG and PG-dopa10% nanoparticles from Fig. 3(c) and (d).



topography images (Fig. S2, ESI<sup>†</sup>). It should be noted that the AFM measurements were done in a dry state, which were then compared to cryo-transmission electron microscopy (TEM) and dynamic light scattering (DLS) which were in frozen and liquid water, respectively. Cryo-TEM images of PG and PG-dopa10% nanoparticles (Fig. 2(c) and (d), respectively) revealed the shape of the nanoparticles at high resolution, which are consistent with an irregular sphere. DLS revealed a shift in the intensity peak towards larger hydrodynamic diameters, where the *Z*-average diameter increased from ~72 nm to ~110 nm, and the dispersity (PDI) also increased from 0.084 to 0.239 (Table S1, ESI<sup>†</sup>). Given the bias of DLS towards larger particles, we computed the average diameters of both particle types from the cryo-TEM images (Fig. 2(f)). We found that the PG nanoparticles had diameters in the range of 40 nm to 45 nm, whereas for PG-dopa10% this increased slightly towards 50 nm to 55 nm. This indicated the average size increased after modification. Furthermore, the column graph shape of PG nanoparticles was sharper than that of PG-dopa10% nanoparticles, indicating that the size distribution also increased after modification. This trend was consistent with the diameter population distribution curve from DLS measurements (Fig. 3(e)). The graph shows the relative intensity of scattering light of the nanoparticles with different sizes. We note that the diameters between cryo-TEM and DLS are different in definition (observable size *vs.* hydrodynamic size). The PG-dopa10% nanoparticles were found to be negatively charged with a zeta potential of -15.0 mV, possibly due to the deprotonation of the catechol groups. The negative charge can aid the nanoparticle stability in water.

### Morphology and thickness of the PG-dopa10% coating

Scanning electron microscopy (SEM) was used to observe the PG-dopa10% coating on silicon wafers. The coating was continuous and smooth (the left area of Fig. 3(a)), whereas the edge of the film (limit of the dip-coating) was porous, with some aggregate nanoparticles. This indicated that the PG-dopa10% nanoparticles showed affinity to the silica material and the interactions between nanoparticles are negligible. The AFM topography image revealed that a continuous, dense PG-dopa10% coating of ~18 nm in thickness formed on the silicon wafer by dip coating into the PG-dopa10% water dispersion (Fig. 3(b) and (c)). The thickness of the PG-dopa10% coating was slightly larger than the height of individual PG-dopa10% nanoparticles (~12 nm) (Fig. S2, ESI<sup>†</sup>), from AFM topography images but less than the double height of the nanoparticles. To obtain further insight into the structure of PG-dopa and PG-dopa coating, wide-angle X-ray scattering and X-ray reflectivity measurements were performed using established methods.<sup>26</sup> Fig. S3a and b (ESI<sup>†</sup>) shows the amorphous nature of the PG-dopa10% which is significantly different from crystalline cellulose fibres. The obtained X-ray reflectivity curves together with its corresponding fit data are shown in Fig. S4 (ESI<sup>†</sup>). The weakly damped Kiessig fringes observed throughout the curve indicated a relatively smooth surface with a uniform coating thickness. A good fit of the experimental curve was

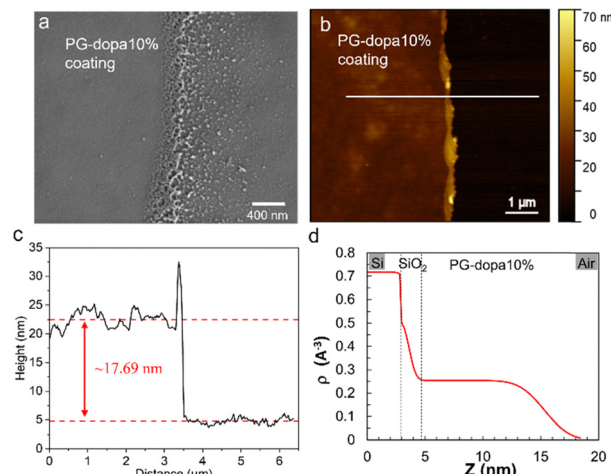


Fig. 3 (a) The SEM image of the PG-dopa10% coating on the silicon wafer prepared by dip coating (the left part is the coating and the edge of the coating is in the middle). (b) The AFM topography image of a scratch of the PG-dopa10% coating on the silicon wafer. (c) The height of the white line in the AFM topography image. (d) XRR curve of the PG-dopa coating on the silicon wafer. The inset shows the electron density profile extracted from the best fit of the XRR curve.

obtained using a single-layer model onto a thin native silicon oxide layer with a thickness of 0.74 nm. The electron density profile used to obtain the best fit (Fig. 3(d)) corroborates the uniformity of the coating with a thickness and a RMS roughness of 11.7 nm and 1.7 nm, respectively.

### The underwater adhesion performance of PG-dopa coatings

The colloidal probe AFM technique was used to characterize the adhesion properties of the underwater PG-dopa10% coating (Fig. 4(a)). A colloidal probe (spherical silica particles with a 20 μm diameter) was brought into contact with PG-dopa coatings on glass substrates, and the force–distance curves were recorded, in water solution. Fig. 4(b) shows a schematic representation of the force distance curve from our experiments. The contact time as well as the maximal load on the cantilever and the retraction rate were varied. As shown previously, the thermodynamic work of adhesion in the case of the interactions of soft polymeric bodies is often very challenging to measure due to the very rapid pull-off event and requires specific experimental setups that are not suitable for every experimental system.<sup>27</sup> In order to avoid misunderstanding, we use here the strain energy release rate *G* instead of the work of adhesion, as we use a pull-off experiment to determine the adhesion properties of the PG-dopa coatings. The strain energy release rate *G*, the area on the retraction part of the force–distance curve (Fig. S6, ESI<sup>†</sup>) below zero normalized on the calculated area of contact, was used to characterize the adhesion performance of the PG-dopa coatings (Fig. 4(c) and (d)).

In the case of the interaction of soft bodies, the increase of adhesion on contact time, retraction rate, and maximal load is very common.<sup>27–30</sup> A longer contact time allows additional bonds and interactions between the two surfaces to develop. Larger maximal loads increase the deformation of the soft

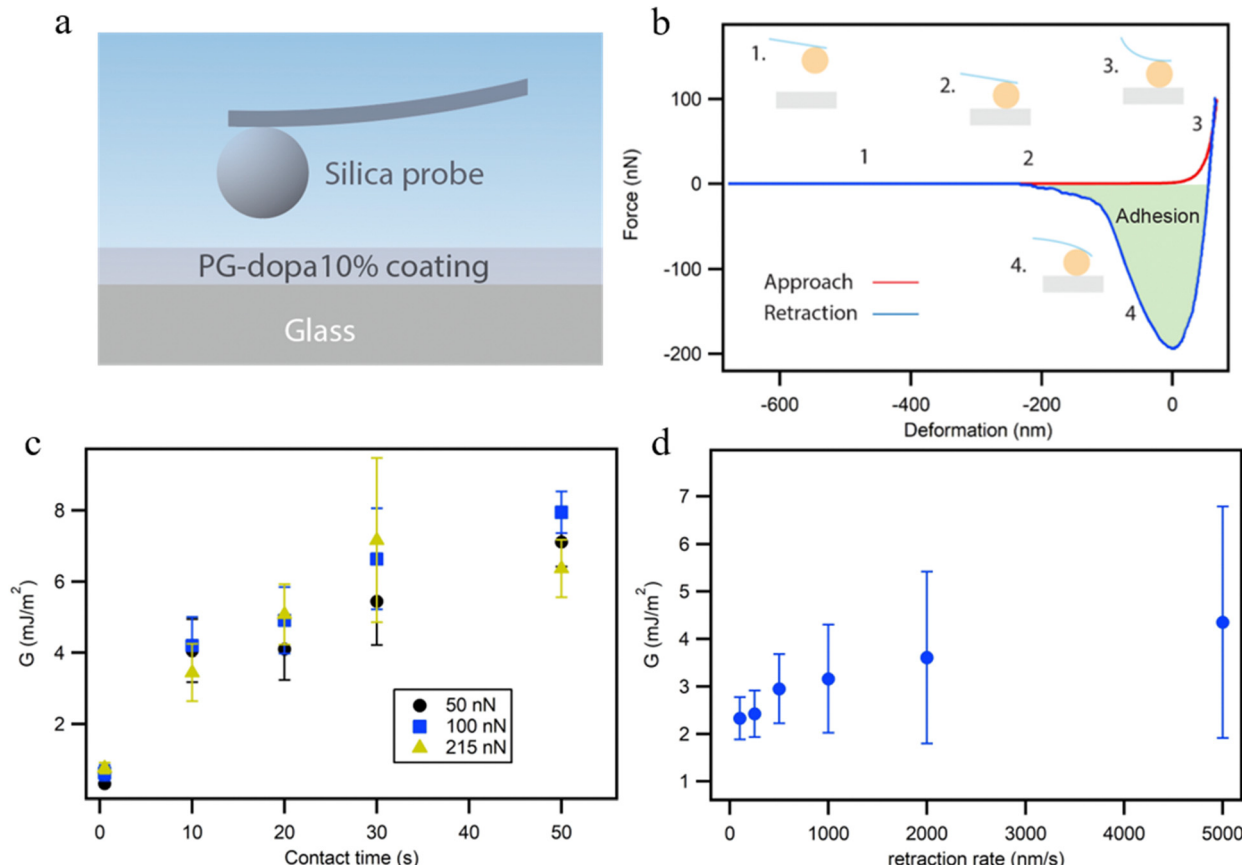


Fig. 4 (a) Schematic of the colloidal probe AFM measurement setup. (b) A typical force-deformation approaching and retraction curve from our colloidal probe AFM experiment of PG-dopa10% films. (c) The strain energy release rate  $G$  of PG-dopa10% coating dependence on contact time for the maximal load force. (d) Strain energy release rate of the PG-dopa10% coating as a function of retraction rate.

bodies, thereby increasing the contact area and the total number of bonds between the two surfaces. Higher retraction rates are connected with the higher rates for the separation of two surfaces influencing the pull-off force drastically.<sup>31,32</sup> In our case, the increase of the contact time results in a drastic increase of  $G$  from below  $1 \text{ mJ m}^{-2}$  to around  $7 \text{ mJ m}^{-2}$  on average for each maximal load used (Fig. 5(c)).

While the data for the influence of the retraction rate on  $G$  have a large standard deviation due to the deposition of the matter on the colloidal probe, which is inevitable in the case of the single particle experiment, the trends can still be seen. The average values of  $G$  more than doubled from  $100 \text{ nm s}^{-1}$  to  $5000 \text{ nm s}^{-1}$ .

The influence of the maximal load, however, was insignificant in our case. The reason for this behavior can be understood by comparing the maximum deformation of the PG-dopa10% coating generated at each maximal load (Fig. S5, ESI†). The increase of the maximal load did not result in a substantial increase in the deformation. The load applied to a soft deformable surface causes a certain amount of deformation. The simplest theory describing the relationship between the applied load  $F$  and the resulting deformation  $\delta$  is the Hertz model. According to this model,  $F \sim \delta^{3/2}$ . Therefore, an increase in load should cause additional deformation. The fact

that the deformation remains the same and is not zero suggests that a very hard substrate (*i.e.*, glass) is covered by a relatively soft layer. This layer is deformed until the colloidal probe reaches the glass substrate. After this, the cantilever is too soft to indent and measure the deformation of the glass and the silica colloidal probe. Therefore, a maximal load of 50 nN was sufficient to reach the glass substrate under the PG-dopa10% coating. The resulting values of the maximum deformation in this case can be used as an indication of the thickness of the PG-dopa10% coating under water. The maximum deformation of the coating was around 75 nm (Fig. S5, ESI†), which is consistent with the nanoparticle size from the DLS measurements.

The adhesion performance of the different PG-dopa coatings was also characterized, namely PG-dopa5% and PG-dopa15% (Fig. S7, ESI†). PG-dopa5% showed very low adhesion and made the interactions of the colloidal probe with the substrate weaker than in the case of the borosilicate glass (data not shown). PG-dopa15% showed comparable performance to PG-dopa10% at all contact times except 50 s, where the adhesion of PG-dopa15% was about 50% greater than that of PG-dopa10%. However, comprehensive investigation of the adhesion performance of PG-dopa15% was limited by the very high colloidal probe contamination, which was significantly greater than that of PG-dopa10%. The thickness of PG-dopa15% was close to that of



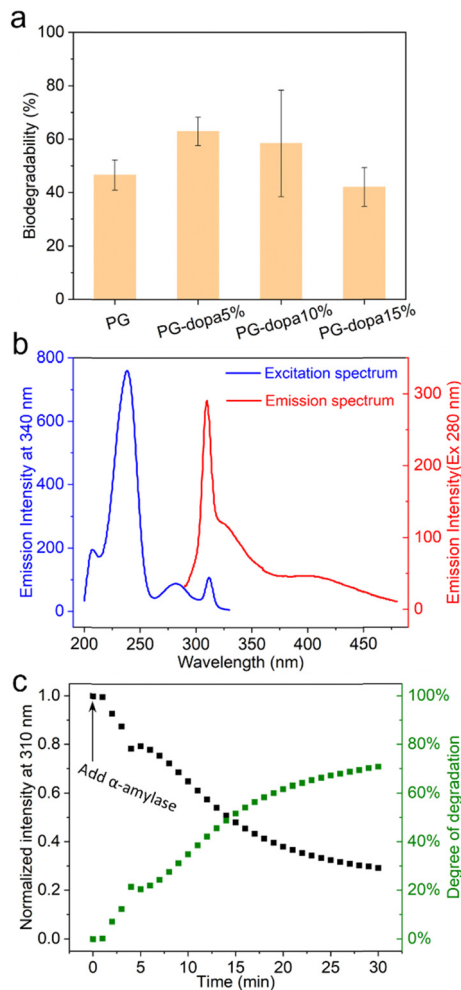


**Fig. 5** (a) The degradation of PG and PG-dopa nanoparticles in 1 U  $\alpha$ -amylase PBS solution after 3 h. (b) Fluorescence excitation and emission spectra of PG-dopa10% films. (c) PG-dopa10% coated quartz incubated in  $\alpha$ -amylase ( $45 \text{ U mL}^{-1}$ ) PBS solution, with fluorescence intensity monitored as a function of time. The excitation and emission wavelengths are 280 nm and 310 nm.

PG-dopa5% and less than that of PG-dopa10% (Fig. S8 and S9, ESI<sup>†</sup>). An increased tendency for colloidal probe contamination in the case of PG-dopa15% and lower thickness compared to PG-dopa10% may indicate the lower layer uniformity and stability of PG-dopa15%.

#### Degradation of PG-dopa nanoparticles and PG-dopa10% coatings

The degradation of PG and PG-dopa nanoparticles in a 1 U  $\text{mL}^{-1}$   $\alpha$ -amylase PBS solution (pH 7.4, 0.01 M) over 3 h was assessed using a phenol-sulfuric acid assay (Fig. 5(a)). It was found that the functionalized PG-dopa nanoparticles retained good biodegradability towards  $\alpha$ -amylase as the starting material PG nanoparticles. The PG-5% and PG-10% nanoparticles even showed a higher degradation degree than PG nanoparticles, perhaps due to modifications in the branching structure due to the synthetic additions. To glean insight into

the degradability of the PG-dopa films, a different assay was needed, due to an inability to ascertain the exact amount of PG-dopa10% in the films. We found that the PG-dopa10% has fluorescence properties, whereby under 280 nm excitation, significant fluorescence was observed, peaking at 310 nm (Fig. 5(b)). This emission maximum at 310 nm was used to assess the degradability of the films in real-time, after soaking in  $\alpha$ -amylase ( $45 \text{ U mL}^{-1}$ ) solution (Fig. 5(c)). It was found that there was a kinetic decrease in the fluorescence of the film, decreasing from  $\sim 1800$  counts and saturating at about  $\sim 500$  counts after 30 minutes. This highlights that the adhesive PG-dopa materials are still biodegradable towards glucosidase enzymes with time.

The lyophilised PG-dopa10% was found to be stable under refrigeration for years. The color of the PG-dopa10% water dispersion changed from white foggy to slightly brown (Fig. S10a, ESI<sup>†</sup>) because of the gradual oxidization of the catechol groups.<sup>33</sup> However, no aggregated particles were observed from DLS measurements after storing in the 4 °C fridge for a week or 9 months (Fig. S10b, ESI<sup>†</sup>). The reason for decreasing PG-dopa10% particle sizes after 9 months might be the degradation of the glycogen nanoparticles over time.

Together, these underwater adhesive nanoparticles can offer a renewable biomaterial alternative to highly synthetic mussel-foot protein mimics, where the degradability yields glucose and a small amount of dopamine. Our study has focused on contact between ideal surfaces (plane and smooth sphere) and how it changes between rough surfaces is not yet known. Furthermore, the adhesiveness towards other materials, such as soft, elastic tissues, is currently the subject of our future investigations.

## Conclusions

We have reported on the synthesis of phytoglycogen-dopamine hybrid materials. The catechol group of dopamine endowed the phytoglycogen nanoparticles with an ability to adhere to underwater silicon dioxide materials. It was shown that the phytoglycogen-dopamine nanoparticles adsorbed readily and densely onto silicon dioxide substrates, forming continuous monolayers from a water dispersion. The thickness of the coating was found to be  $\sim 18$  nm in the dry state and  $\sim 78$  nm when solvated. The adhesive properties of the coating were striking, with a maximum strain energy release rate of  $7.2 \text{ mJ m}^{-2}$  when contacting surfaces of underwater silicon dioxide. Moreover, the modification did not affect the biodegradability of phytoglycogen. This sticky phytoglycogen coating might find applications in short-term implantable devices or as “micro” adhesives for the assembly of nanoparticles.

## Data availability

The authors confirm that the data supporting the findings of this study are available within the article.

## Conflicts of interest

There are no conflicts to declare.

## Acknowledgements

We sincerely thank Dr. Petr Formanek and Michael Göbel for assistance with TEM and SEM measurements, respectively, and Dr. Hartmut Komber for NMR measurements. The authors additionally would like to thank Dr. Alexander Münch, Qiong Li and Dr. Ilka Hermes for their help with UV-vis spectroscopy and AFM measurements, and Thomas Witzmann and Dr. Günter Auernhammer for discussions. Prof. Mahmoud Al-Hussein thanks the University of Jordan and Leibniz-Institut for Polymer Research Dresden (IPF Dresden) for financial support. This work received funding from the European Union's Horizon 2020 research and innovation program under the Marie Skłodowska-Curie grant agreement 872233 ("PEPSA-MATE"). J. L. gratefully acknowledges the Chinese Scholarship Council (CSC) for funding.

## References

- 1 E. W. Danner, Y. Kan, M. U. Hammer, J. N. Israelachvili and J. H. Waite, *Biochemistry*, 2012, **51**, 6511–6518.
- 2 J. H. Waite and X. Qin, *Biochemistry*, 2001, **40**, 2887–2893.
- 3 H. Lee, N. F. Scherer and P. B. Messersmith, *Proc. Natl. Acad. Sci. U. S. A.*, 2006, **103**, 12999–13003.
- 4 H. Lee, S. M. Dellatore, W. M. Miller and P. B. Messersmith, *Science*, 2007, **318**, 426–430.
- 5 M. A. North, C. A. Del Grosso and J. J. Wilker, *ACS Appl. Mater. Interfaces*, 2017, **9**, 7866–7872.
- 6 J. Yu, B. Cheng and H. Ejima, *J. Mater. Chem. B*, 2020, **8**, 6798–6801.
- 7 B. Cheng, J. Yu, T. Arisawa, K. Hayashi, J. J. Richardson, Y. Shibuta and H. Ejima, *Nat. Commun.*, 2022, **13**, 1892.
- 8 R. Cui, F. Chen, Y. Zhao, W. Huang and C. Liu, *J. Mater. Chem. B*, 2020, **8**, 8282–8293.
- 9 Z. Du, F. Qiao, L. Tong, W. Zhang, X. Mou, X. Zhao, M. F. Maitz, H. Wang, N. Huang and Z. Yang, *The Innovation*, 2024, **5**, 100671.
- 10 Q. A. Besford, *Soft Matter*, 2024, **20**, 3577–3584.
- 11 N. Davydiuk, V. Londhe, M. F. Maitz, C. Werner, A. Fery and Q. A. Besford, *Nanoscale*, 2025, **17**, 252–260.
- 12 Q. A. Besford, F. Cavalieri and F. Caruso, *Adv. Mater.*, 2020, **32**, 1904625.
- 13 T. Isogai, T. Saito and A. Isogai, *Biomacromolecules*, 2010, **11**, 1593–1599.
- 14 S. A. Engelberth, N. Hempel and M. Bergkvist, *Bioconjugate Chem.*, 2015, **26**, 1766–1774.
- 15 M. Rabyk, M. Hraby, M. Vetrík, J. Kucka, V. Proks, M. Parizek, R. Konefal, P. Krist, D. Chvatil, L. Bacakova, M. Slouf and P. Stepanek, *Carbohydr. Polym.*, 2016, **152**, 271–279.
- 16 M. Perrone, A. Lopalco, A. Lopedota, A. Cutrignelli, V. Laquintana, J. Douglas, M. Franco, E. Liberati, V. Russo, S. Tongiani, N. Denora and A. Bernkop-Schnürch, *Eur. J. Pharm. Biopharm.*, 2017, **119**, 161–169.
- 17 P. Pacchin Tomanin, J. Zhou, A. Amodio, R. Cimino, A. Glab, F. Cavalieri and F. Caruso, *J. Mater. Chem. B*, 2020, **8**, 4851–4858.
- 18 S. Arias, S. Amini, J. Horsch, M. Pretzler, A. Rompel, I. Melnyk, D. Sychev, A. Fery and H. G. Börner, *Angew. Chem., Int. Ed.*, 2020, **59**, 18495–18499.
- 19 H.-J. Butt, *Biophys. J.*, 1991, **60**, 1438–1444.
- 20 W. A. Ducker, T. J. Senden and R. M. Pashley, *Nature*, 1991, **353**, 239–241.
- 21 Y. Jiang and K. T. Turner, *Extreme Mech. Lett.*, 2016, **9**, 119–126.
- 22 J. L. Hutter and J. Bechhoefer, *Rev. Sci. Instrum.*, 1993, **64**, 1868–1873.
- 23 K. L. Johnson, K. Kendall, A. D. Roberts and D. Tabor, *Proc. R. Soc. London, Ser. A*, 1971, **324**, 301–313.
- 24 Q. A. Besford, A. C. G. Weiss, J. Schubert, T. M. Ryan, M. F. Maitz, P. P. Tomanin, M. Savioli, C. Werner, A. Fery, F. Caruso and F. Cavalieri, *ACS Appl. Mater. Interfaces*, 2020, **12**, 38976–38988.
- 25 M. Bertoldo, G. Zampano, L. Suffner, E. Liberati and F. Ciardelli, *Polym. Chem.*, 2013, **4**, 653–661.
- 26 M. Al-Hussein, Y. Séréro, O. Konovalov, A. Mourran, M. Möller and W. H. de Jeu, *Macromolecules*, 2005, **38**, 9610–9616.
- 27 D. Sychev, S. Schubotz, Q. A. Besford, A. Fery and G. K. Auernhammer, *J. Colloid Interface Sci.*, 2023, **642**, 216–226.
- 28 I. U. Vakarelski, A. Toritani, M. Nakayama and K. Higashitani, *Langmuir*, 2001, **17**, 4739–4745.
- 29 R. Buzio, A. Bosca, S. Krol, D. Marchetto, S. Valeri and U. Valbusa, *Langmuir*, 2007, **23**, 9293–9302.
- 30 D. Pussak, D. Ponader, S. Mosca, T. Pompe, L. Hartmann and S. Schmidt, *Langmuir*, 2014, **30**, 6142–6150.
- 31 D. Maugis and M. Barquins, *J. Phys. D: Appl. Phys.*, 1978, **11**, 1989.
- 32 A. N. Gent and J. Schultz, *J. Adhes.*, 1972, **3**, 281–294.
- 33 J. Ju, S. Jin, S. Kim, J. H. Choi, H. A. Lee, D. Son, H. Lee and M. Shin, *ACS Appl. Mater. Interfaces*, 2022, **14**, 25115–25125.

